Structural Modelling of Compliance-Based Morphing Structures under Transverse Shear Loading

Andres E. Rivero*, Paul M. Weaver† and Benjamin K.S. Woods ‡
Bristol Composites Institute (ACCIS), University of Bristol, Bristol, United Kingdom, BS8 1TR

A parametrically driven structural model based on Mindlin-Reissner plate theory is developed to capture the three-dimensional deformations of a compliance-based morphing trailing edge device with severe structural discontinuities. This model addresses limitations of a previously developed Kirchoff-Love plate model, where out-of-plane displacements under torsional loading could not be accurately predicted due to unmodelled transverse shear deformations. The model is used to study the Fish Bone Active Camber (FishBAC) device, which is modelled here as a discontinuous plate structure, which captures the sudden changes in stiffness created by the concept geometrical configuration. Courant's penalty method is implemented in the form of artificial penalty springs, to account for stiffness discontinuities. A numerical validation is performed using Finite Element Analysis (FEA). This analytical model represents a robust, efficient, mesh-independent and parameter-driven solution to modelling discontinuous plate structures. These traits make it useful for ongoing fluid-structure interaction analysis and optimisation of the FishBAC concept, and for application to other complex composite structures.

I. Nomenclature

A_{ij}	=	Laminate's membrane stiffness matrix terms
a_i	=	Chordwise length in the x-direction
B_{ij}	=	Laminate's extension-bending coupling stiffness matrix terms
b_j	=	Spanwise length in the y-direction
D_{ij}	=	Laminate's bending stiffness matrix terms
E_{ij}	=	Young's Modulus in the i,j-direction
G_{ij}	=	Shear Modulus in the i,j-direction
ν_{ij}	=	Poisson's Ratio in the i,j-direction
H_{ij}	=	Transverse shear stiffness matrix terms
κ	=	Timoshenko shear correction factor
k_k	=	Artificial penalty spring stiffness
γ_{ij}	=	Transverse shear strain in the i,j-direction
Γ_x	=	Boundary conditions' circulation function
M_x	=	Applied distributed moments
ζ_i	=	Normalised chordwise position
η_j	=	Normalised spanwise position
$\overline{Q}_{ij}$	=	Ply stiffness in the global coordinate system
u^o_{ij}	=	In-plane displacement in the chordwise x-direction
v^o_{ij}	=	In-plane displacement in the spanwise y-direction
w_{ij}	=	Out-of-plane displacement in the through-thickness z-direction
U	=	Strain energy
W	=	Potential energy due to external loads
ψ_x	=	xz-plane rotation
ψ_y	=	yz-plane rotation
$T(\zeta)$	=	Chebyshev polynomials of the first kind
$X(x)$	=	Chebyshev polynomial expansion in the x-direction
$Y(y)$	=	Chebyshev polynomial expansion in the y-direction

*PhD Student, Bristol Composites Institute (ACCIS), Department of Aerospace Engineering. AIAA Student Member.
†Professor in Lightweight Structures, Bristol Composites Institute (ACCIS), Department of Aerospace Engineering. AIAA Member.
‡Lecturer in Aerospace Structures, Bristol Composites Institute (ACCIS), Department of Aerospace Engineering. AIAA Member.

II. Introduction

Morphing structures have been a subject of interest in the aerospace sector in recent years due to their ability to change shape without surface discontinuities. This characteristic makes them attractive for designing adaptive aircraft structures that can continuously change and optimise aerodynamic shapes throughout flight [1]. Among all of the types of morphing techniques applicable to fixed wing aircraft (e.g. span morphing, variable sweep, variable twist, etc.), camber morphing is the most commonly pursued. It is based on the ability to continuously vary aerofoil camber distribution in a smooth and continuous way. This technique represents a better alternative to varying camber using traditional hinged panels (e.g. ailerons, elevator, rudder, etc.) — where changes in camber occur in a sharp, discontinuous manner — as smooth changes in camber provide similar lift coefficient control authority with a much lower drag penalty [2]. Therefore, variable camber offers higher lift-to-drag ratios and lower noise than conventional control surfaces. Furthermore, unlike hinged flaps, camber morphing devices can be designed to vary their camber continuously along the span. This can potentially be used for controlling in real time the spanwise lift distribution, minimising induced drag [3]. It also has significant potential for use as both an active and passive load alleviation device to allow for gust rejection — mitigating critical design cases and allowing for reduced wing mass.

Another attractive aspect of camber morphing is that it is able to achieve large changes in aerodynamic forces and moments with relatively small changes in aerofoil shape, which furthermore can be limited to the trailing edge of the aerofoil. This consideration makes camber morphing attractive in terms of maximising aerodynamic control authority while minimising the structural impact and actuation energy requirements [4].

Variable camber is not a new concept as it dates from 1920s and 1930s, where several camber morphing mechanisms were presented and patented [5–7]. These concepts were not successfully implemented however, likely due in part to the use of heavy and complex mechanisms, which made them unattractive for conventional applications. Due to advances in smart materials and structures, there have a new research drive — in the past two decades — towards developing novel camber morphing concepts. Specifically, one area of research focus has been on smart material actuation — including using piezoelectric actuators [8, 9], shape memory alloys (SMAs) [3, 10], exploiting bistability in composite laminates [11, 12] — and also on shape optimisation [13, 14].

One of the first "modern" morphing concepts was the NASA's F-111 Mission Adaptive Wing [15], which implemented a sliding and bending skins over internal linkage mechanisms to achieve smooth leading and trailing edge camber deflections. Other highlighted concepts are the DARPA Smart Wing, where a combination of a plate structure with honeycomb and silicone is used [16]; the Flexys Flexfoil^{TM}, which can achieve a $\pm 10^{\circ}$ transverse trailing edge deflection, as well as twist; the DLR Belt-Rib concept [17] and the Fish Bone Active Camber (FishBAC) device [18], which is the subject of study in this work.

The Fish Bone Active Camber (FishBAC) is a morphing trailing edge device capable of achieving large, smooth and continuous changes in camber without surface discontinuities (Fig. 1) It consists of a central bending plate (the spine) that carries most of the loads and a series of spanwise stringers that support an elastomer skin. The stringers are designed to provide a high level of spanwise rigidity without adding significant chordwise stiffness and also serve to maintain the aerofoil's thickness distribution during morphing. The elastomer skin is pre-tensioned before bonding to significantly increase out-of-plane stiffness (thereby reducing deformations under aerodynamic pressure loading) and to avoid skin buckling when in compression. The structure is actuated using antagonistic fabric tendons that transfer the actuation loads from a driving pulley to the trailing edge of the spine (Fig. 2). Current designs include two servo-based actuation points along the span, at equidistant points from the centre of the wing. However, these are open design variables; the number and location of actuation points and type of actuators can be modified in accordance to design requirements, and the concept is actuator agnostic — it will work with any type of actuator capable of generating rotational output.

Because of its geometrical configuration — a chordwise compliant spine with intermittent spanwise stringers and a compliant elastomer skin as the outer surface — the FishBAC is highly anisotropic: it is significantly more compliant in the chordwise direction than in the spanwise. This allows it to obtain large and continuous changes in camber with low actuation energy requirements, while providing significant spanwise rigidity. Furthermore, recent work has shown that using carbon fibre-reinforced polymer (CFRP) laminates in the FishBAC spine allows for further amplification of this anisotropic nature and adds another degree of freedom to the tailorability of structural stiffness [19].

To analyse and design a carbon fibre wind tunnel model, a two-dimensional structural model capable of analysing composites laminates is needed. Therefore, a Kirchhoff-Love based plate theory model was developed in previous work by the authors [20] to analytically model the static behaviour of a composite FishBAC under transverse pressure and actuation loads. Although successful in predicting deflections under uniform transverse pressure and uniform actuation loads (when validated against Finite Element Analysis), the model fails to accurately predict deflections when the FishBAC is subject to spanwise twist due to non-uniform actuation loads. The authors showed that this limitation is due

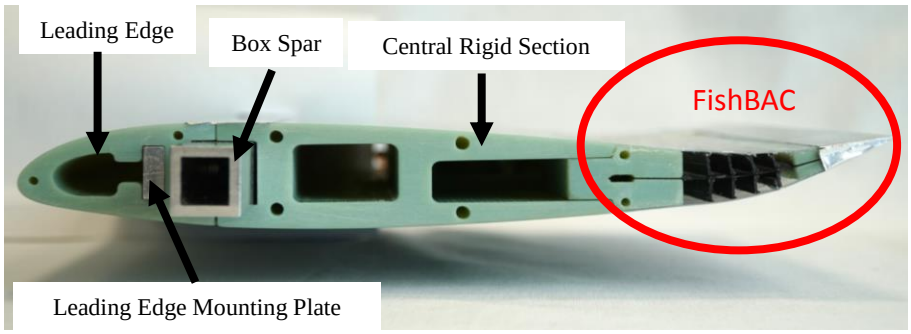

Fig. 1 Wind tunnel wing model with composite FishBAC trailing edge device

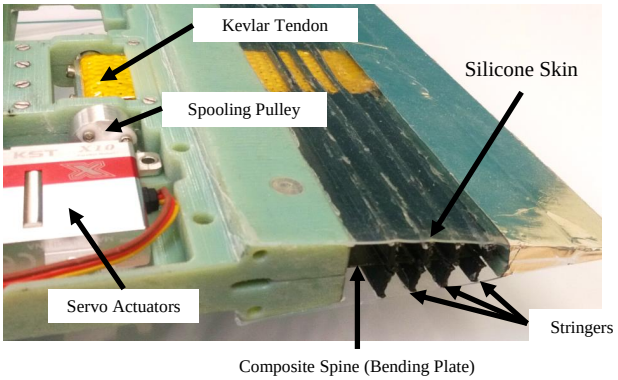

Fig. 2 FishBAC structure and actuation mechanism

to the existence of transverse shear strains due to torsion, which cannot be predicted using Kirchhoff-Love plate theory, which completely neglects transverse shear strains.

The objective of this work is to address these limitations and enhance the modelling technique proposed by Rivero et al. [20]. This is achieved by implementing Mindlin-Reissner plate theory, which models transverse shear deformations by applying a First-Order Shear Deformation Theory (FSDT), which assumes that transverse shear displacements vary linearly across the thickness of the structure [21]. This enhanced analytical structural model is validated against Finite Element Analysis (FEA). The model is implemented using MATLAB®R2016a, while the FEA validation is performed using ABAQUS/CAE®6.14-1.

The novelty of this work resides on its ability to capture displacements of a highly discontinuous plate structure subjected to different load cases (including transverse shear loads) using a series of individual plates that are joined together using artificial penalty springs. This model will become a key element in future design, optimisation and fluid-structure interaction of the FishBAC. Moreover, its use is not exclusive to the FishBAC device; any continuous or discontinuous composite plate structure can be modelled using this technique. This article first introduces the modelling technique, including the solution method, boundary conditions and assumptions. Furthermore, it introduces the Finite Element Analysis validation technique, followed by a summary of results and an analysis on the numerical performance of the model.

III. Analytical Structural Model

The analytical structural model that is developed in this article is based on the Rayleigh-Ritz Method, which is used to solve the plate differential equation using a weak formulation. Furthermore, Classical Laminate Theory (CLT) extended for Mindlin-Reissner plates is used to calculate the stiffness terms [22]. This solution technique requires the use of assumed shape functions, in this case, the authors have selected Chebyshev Polynomials of the First Kind. Lastly, to account for the large number of chordwise and spanwise stiffness discontinuities due to the presence of stringers and discrete actuation inputs, the structure is discretised in sections of uniform stiffness that are joined using the Courant's penalty method in the form of artificial springs [23].

A. Mindlin-Reissner Plate Theory

In beam analysis, Euler-Bernoulli beam theory is unable to predict deflections of thick beams. This is due to its inability to account for transverse shear deformations and, therefore, Timoshenko beam theory was introduced to account for transverse shear deformations [24].

Similarly, Kirchhoff-Love plate theory is analogous to Euler-Bernoulli beam theory and it fails to model the behaviour of thick plates as it assumes no through-thickness shear deformations. Therefore, the Mindlin-Reissner Plate Theory extends Kirchhoff-Love Plate Theory to include the effects of transverse shear deformation by allowing the through-thickness normal planes to rotate. It assumes that transverse shear displacements vary linearly across the thickness of the plate, which is why it is also known as the First-Order Shear Deformation Theory of Plates (FSDT) [25].

In order to solve the Mindlin-Reissner equations with the Rayleigh-Ritz Method, a strain energy formulation of the plate's differential equation is needed. This equation considers total strain energy in the plates as the summation of strain energies due to stretching and bending (Eq. (1)) and transverse shear (Eq. (2)), defined as [22, 26]:

$$\begin{aligned} U_{KL} = \frac{1}{2}\iint & A_{11}\left(\frac{\partial u^o}{\partial x}\right)^2 + 2A_{12}\frac{\partial u^o}{\partial x}\frac{\partial v^o}{\partial y} + A_{22}\left(\frac{\partial v^o}{\partial y}\right)^2 + 2\left(A_{16}\frac{\partial u^o}{\partial x} + A_{26}\frac{\partial v^o}{\partial y}\right)\left(\frac{\partial u^o}{\partial y} + \frac{\partial v^o}{\partial x}\right) + A_{66}\left(\frac{\partial u^o}{\partial y} + \frac{\partial v^o}{\partial x}\right)^2 \\ & - 2B_{11}\frac{\partial u^o}{\partial x}\frac{\partial \psi_x}{\partial x} - 2B_{22}\frac{\partial v^o}{\partial y}\frac{\partial \psi_y}{\partial y} - 2B_{12}\left(\frac{\partial v^o}{\partial y}\frac{\partial \psi_x}{\partial x} + \frac{\partial u^o}{\partial x}\frac{\partial \psi_y}{\partial y}\right) - 2B_{66}\left(\frac{\partial u^o}{\partial y} + \frac{\partial v^o}{\partial x}\right)\left(\frac{\partial \psi_x}{\partial y} + \frac{\partial \psi_y}{\partial x}\right) \\ & - 2B_{16}\left[\frac{\partial \psi_x}{\partial x}\left(\frac{\partial u^o}{\partial y} + \frac{\partial v^o}{\partial x}\right) + \frac{\partial u^o}{\partial x}\left(\frac{\partial \psi_x}{\partial y} + \frac{\partial \psi_y}{\partial x}\right)\right] - 2B_{26}\left[\frac{\partial \psi_y}{\partial y}\left(\frac{\partial u^o}{\partial y} + \frac{\partial v^o}{\partial x}\right) + \frac{\partial v^o}{\partial y}\left(\frac{\partial \psi_x}{\partial y} + \frac{\partial \psi_y}{\partial x}\right)\right] + D_{11}\left(\frac{\partial \psi_x}{\partial x}\right)^2 \\ & + D_{22}\left(\frac{\partial \psi_y}{\partial y}\right)^2 + D_{66}\left(\frac{\partial \psi_x}{\partial y} + \frac{\partial \psi_y}{\partial x}\right)^2 + 2D_{12}\left(\frac{\partial \psi_x}{\partial x}\frac{\partial \psi_y}{\partial y}\right) + 2D_{16}\frac{\partial \psi_x}{\partial x}\left(\frac{\partial \psi_x}{\partial y} + \frac{\partial \psi_y}{\partial x}\right) + 2D_{26}\frac{\partial \psi_y}{\partial y}\left(\frac{\partial \psi_x}{\partial y} + \frac{\partial \psi_y}{\partial x}\right) dx\, dy \end{aligned} \tag{1}$$

$$U_{MR} = \frac{1}{2}\iint \left[H_{44}\left(\frac{\partial w}{\partial y} - \psi_y\right)^2 + 2H_{45}\left(\frac{\partial w}{\partial y} - \psi_y\right)\left(\frac{\partial w}{\partial x} - \psi_x\right) + H_{55}\left(\frac{\partial w}{\partial x} - \psi_x\right)^2\right] dx\, dy, \tag{2}$$

where A_{ij}, B_{ij},D_{ij} and H_{ij} matrices are the plate's material and geometric stiffness, u^o, $v^o$and w are the plate displacements and ψ_x and ψ_y are the plate rotations. Note the subscript *KL* in Eq. (1) denotes the strain energy terms present in Kirchoff-Love theory, whereas the subscript *MR* in Eq. (2) denotes the additional term added by Mindlin-Reissner theory to capture the transverse shear energy. These plate rotations include transverse shear strains, such that:

$$\psi_x = \frac{\partial w}{\partial x} - \gamma_{xz} \qquad \text{and} \qquad \psi_y = \frac{\partial w}{\partial y} - \gamma_{yz} \quad . \tag{3}$$

The A_{ij},B_{ij} and D_{ij} terms in Eq. (1) — commonly known as the *ABD* matrix — are, respectively, the extension, bending-coupling and bending material and geometric stiffness of the laminate, and these are obtained using Classical Laminate Theory (CLT) [27]. Furthermore, the H_{ij} terms in Eq. (2) correspond to the transverse shear stiffness, and are derived from

$$H_{ij} = \frac{1}{\kappa}\int_h \overline{Q}_{ij}\, dz = \frac{1}{\kappa}\sum_{k=1}^{K} \overline{Q}_{ij,k}(z_k - z_{k-1})\, dz\,, \tag{4}$$

where $i, j = 4, 5$ and κ is known as the Timoshenko Shear Correction Factor, which has an approximate value of $6/5$ for rectangular cross-sections. Although this approximation is valid for isotropic plates, it has been shown to provide accurate results when used to model composite laminates [26]. Therefore, a value of $\kappa = 6/5$ is used throughout this study. Lastly, the $\overline{Q}_{ij}$ terms correspond to the stiffness of each ply in the global coordinate frame, which are a function of fibre orientation angle and the following material properties: E_{11}, E_{22}, ν_{12}, G_{12}, G_{13} and G_{23}, in which the subscripts $i, j = 1, 2, 3$ refer to the fibre, transverse and trough-thickness directions, respectively.

B. Shape Functions and Boundary Conditions

When solving the plate equation by minimising total energy (i.e. by using Rayleigh-Ritz Method), the displacements and transverse shear strains of the plate are unknown — and become the independent variables of the equation. Therefore, the underlying shape functions of the displacements and transverse shear strains need to be assumed, such that the corresponding amplitudes can be solved for. Commonly, when in 2-D, these are assumed in the form of a double summation in x and y. Therefore, the three displacements become (Eq. (5))

$$u^0_{ij} = \sum_{m=0}^{M}\sum_{n=0}^{N} O^{ij}_{mn} X^i_m(x) Y^j_n(y)\ , \quad v^0_{ij} = \sum_{m=0}^{M}\sum_{n=0}^{N} P^{ij}_{mn} X^i_m(x) Y^j_n(y) \quad \text{and} \quad w_{ij} = \sum_{m=0}^{M}\sum_{n=0}^{N} R^{ij}_{mn} X^i_m(x) Y^j_n(y)\ , \tag{5}$$

and the transverse plane rotations have a similar form (Eq. (6))

$$\psi_x = \sum_{m=0}^{M}\sum_{n=0}^{N} S_{mn}^{ij} X_m^i(x) Y_n^j(y) \quad \text{and} \quad \psi_y = \sum_{m=0}^{M}\sum_{n=0}^{N} V_{mn}^{ij} X_m^i(x) Y_n^j(y) \ . \tag{6}$$

These shape functions described in Eqs. (5-6) have two main components: the assumed shape functions $X(x)$ and $Y(y)$ and the unknown amplitudes O_{ij}, P_{ij}, R_{ij}, S_{ij} and V_{ij}. In plate mechanics, two main types of shape functions are used: periodic functions (e.g. cosine and sine Fourier series) and non-periodic functions (e.g. spline functions and orthogonal polynomials). In this study, orthogonal polynomials are chosen as the assumed shape functions because, unlike simpler formulations, they can successfully predict deflections when a high degree of anisotropy exists. Specifically, the type of orthogonal polynomials that are implemented are the Chebyshev Polynomials of the First Kind, which are defined as Eq. (7)

$$T(\zeta) = \frac{1}{2}\left[\left(\zeta - \sqrt{\zeta^2 - 1}\right)^n + \left(\zeta + \sqrt{\zeta^2 - 1}\right)^n\right], \tag{7}$$

where n corresponds to the polynomial order. This selection is motivated by Rivero et al. [20], where the authors explain that Chebyshev Polynomials of the First Kind allow for direct integration in a normalised domain without leading to values of zero. It is important to note that these polynomials are defined in a normalised domain, therefore, the global coordinate system is transformed into a local coordinate system (Fig. 3) by using the following relationship (Eq. (8)):

$$\zeta_i = \frac{2x_i}{a_i} \quad \text{and} \quad \eta_j = \frac{2y_j}{b_j} \quad . \tag{8}$$

Lastly, it is important to implement the correct boundary conditions. In this particular application, the FishBAC is modelled as a cantilever plate that is clamped at one of its chordwise edges. It can be observed in Fig. 4 that Chebyshev Polynomials do not naturally meet this condition function, as they have non-zero displacements at the boundaries. Therefore, the clamped condition needs to be enforced separately. To achieve this, a circulation function [28] (Eq. (9))

$$\Gamma_x(\zeta) = (\zeta - \zeta_c)^n \, , \tag{9}$$

is added as a multiplier to the displacement and transverse shear functions (i.e. Eqs. (5-6)). This condition forces certain boundary condition at a location ζ_c and the type of boundary condition is set by choosing the value of n. The relevant values for different conditions are given in depth in Table 1. Furthermore, it is important to note that using this circulation function does not affect the orthogonality of the Chebyshev Polynomials — so as long as every polynomial term in the expansion gets multiplied by it.

As the FishBAC structure is modelled as a clamped plate, all three translations u^o, v^o and w and two rotations ψ_x, ψ_y must be equal to zero at the root. However, the transverse shear strains γ_{xz}, γ_{yz} need not be zero, as transverse shear straining at the root is a likely deformation mode [29]. Hence, for a clamped edge, a value of $n = 1$ must be used in Eq. (9), as this yields to zero displacement and rotations at the root, while still allowing for non-zero transverse shear strains at this location.

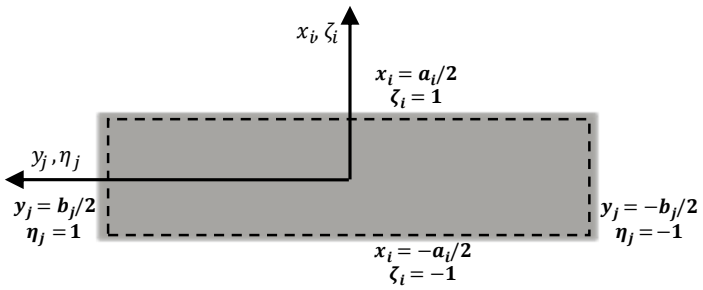

Fig. 3 Example of relationship between normalised and physical coordinate frame

Table 1 Boundary Conditions as implemented by circulation function in Equation (9) [26, 29]

Boundary Condition at ζ_c	$n_{\text{displacement}}$	n_{rotation}	Disp. (u^o, v^o, w)	Rot. (ψ_x, ψ_y)	Transverse Shear Strains $(\gamma_{xz}, \gamma_{yz})$
Free Edge (F)	0	0	Free	Free	Free
Simply Supported (SS)	1	0	0	Free	Free
Clamped (C)	1	1	0	0	Free

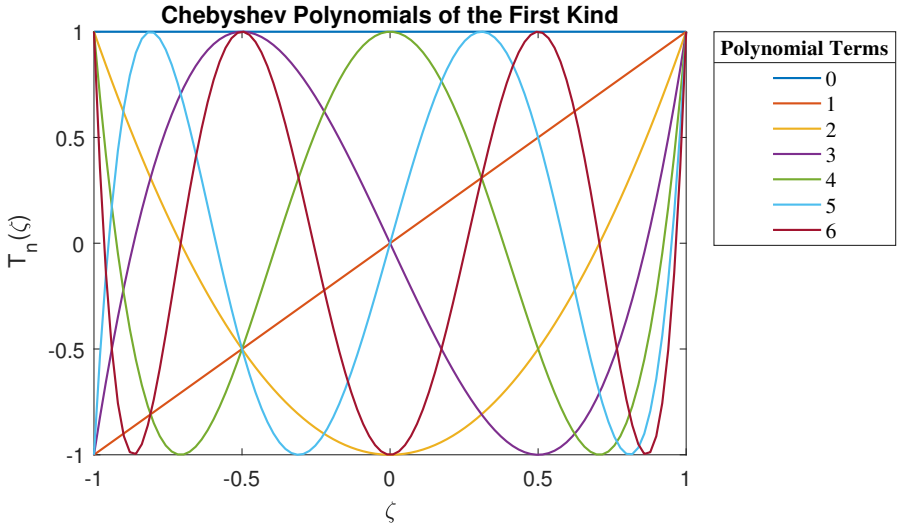

Fig. 4 Chebyshev Polynomials of the First Kind in a normalised domain

The derivatives of the Chebyshev Polynomials that are required to solve Eq. (1) are computed analytically, while all the required integrations in this analytical model are computed numerically using MATLAB's adaptive quadrature functions 'integral' and 'integral2', for 1-dimensional and 2-dimensional integrals, respectively. Because all the integrals are computed in a normalised coordinate system, these can be calculated beforehand and their values can be stored and then transformed to the physical coordinate system, as long as the relationship between the normalised and physical coordinate systems is assumed to be constant (i.e. constant Jacobian). This property allows for significant reduction of the computational cost of running this analytical model as the integrals have to be performed only once "up front" for each set of boundary conditions. This is a significant improvement over the previous approach from Rivero et al. [20], which required "on line" calculation of these integrals.

C. Stiffness Discontinuities

Due to the presence of stringers, the chordwise taper of the aerofoil thickness, and the presence of localised actuation sections along the span, the stiffness of the FishBAC structure is discontinuous. To account for this, the FishBAC structure is modelled in this work as individual plate units of uniform stiffness that are joined together using a series of artificial penalty springs. These penalty springs act by enforcing displacement and rotation continuity at the joints of each partition.

To implement this approach within the Rayleigh-Ritz Method, the strain energy of these artificial springs need to be minimised to enforce displacement and rotation compatibility at joints. The penalty spring energy due to displacements has the form (Eq. (10))

$$U_{pu,kl} = \frac{k_k}{2}\int_{-b_j/2}^{b_j/2}(u_k(x_{kl}^{(+)}, y_j) - u_l(x_{kl}^{(-)}, y_j))^2 dy \;, \quad U_{pv,kl} = \frac{k_k}{2}\int_{-b_j/2}^{b_j/2}(v_k(x_{kl}^{(+)}, y_j) - v_l(x_{kl}^{(-)}, y_j))^2 dy$$
$$\text{and} \qquad U_{pw,kl} = \frac{k_k}{2}\int_{-b_j/2}^{b_j/2}(w_k(x_{kl}^{(+)}, y_j) - w_l(x_{kl}^{(-)}, y_j))^2 dy \tag{10}$$

where k and l refers to two adjacent plate partitions and + and − signs represent the right and left hand sides of the discontinuity (Fig.

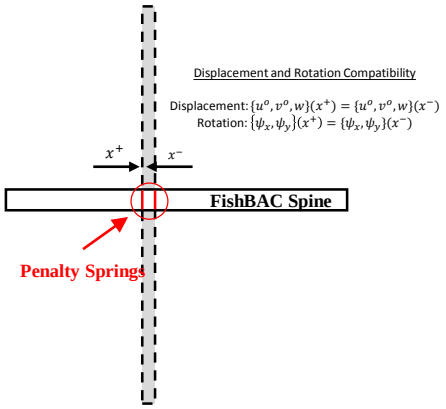

Fig. 5 Displacement and Rotation compatibility enforced at each plate-stringer joint using artificial penalty springs

5), respectively. Similarly, strain energy due to rotation is defined as (Eq. (11))

$$U_{prx,kl} = \frac{k_k}{2}\int_{-b_j/2}^{b_j/2}(\psi_{x_k}(x_{kl}^{(+)}, y_j) - \psi_{x_l}(x_{kl}^{(-)}, y_j))^2 dy \quad \text{and} \quad U_{pry,kl} = \frac{k_k}{2}\int_{-b_j/2}^{b_j/2}(\psi_{y_k}(x_{kl}^{(+)}, y_j) - \psi_{y_l}(x_{kl}^{(-)}, y_j))^2 dy \ . \quad (11)$$

These expressions (Eqs. (10-11)) correspond to penalty springs in the chordwise direction (i.e. along the x-direction). For spanwise partitions along the y-direction, similar equations apply but the integration is performed along the x-direction at $y_k^{(+)}$ and $y_l^{(-)}$ locations.

D. Actuation Loads

As previously mentioned, the composite FishBAC prototype is actuated at two locations along the span of the wing which are equidistant from the centre. This actuation is currently performed by set of two servo actuators, at each actuation point, that drive a tendon spooling pulley. This pulley is connected to a Kevlar tendon tape that travels through slots in the stringers until reaching the trailing edge portion of the composite spine — where it is stitched and bonded directly to the spine. In this way, torque and rotation input to the spooling pulley is transformed into force and displacement of the tendons, before being transformed back into a bending moment at the trailing edge. It is this bending moment which drives the morphing deformation. To capture the impact of this actuation method within this analysis, the external actuation loads are incorporated as an additional source of potential energy. These as modelled as applied distributed moments over each short actuated segment of the FishBAC, according to (Eq. (12))

$$W_{ij} = -\int M_x \, \psi_x(a_i, y)\, dy \ , \quad (12)$$

where a_i is the location where the distributed moment is applied. Note that this neglects any friction on the pulley-tendon system.

E. Rayleigh-Ritz Method: Minimum Potential Energy

As previously mentioned, the solution method that this structural model is based on the principle of conservation of energy. Consequently, without structural frictional losses, the total energy of the system is constant. Differentiating with respect to any of the unknown amplitudes leads to a state of minimum potential energy. If the total energy is defined as the sum of strain energy and potential energy due to external loads (Eq. (13))

$$\Pi(u^0, v^0, w, \psi_x, \psi_y) = U_{KL} + U_{MR} + U_{penalty} + W = \text{constant} \quad , \quad (13)$$

differentiation with respect to the unknown amplitudes O_{mn}^{ij}, P_{mn}^{ij}, R_{mn}^{ij}, S_{mn}^{ij} and V_{mn}^{ij} leads to a state of minimum potential energy — where the right hand side of Eq. (13) is equal to zero. This feature allows a system of $5 \times (M \times N) \times (i \times j)$ independent linear equations to be generated as:

$$\frac{\partial \Pi}{\partial O_{mn}^{ij}}, \frac{\partial \Pi}{\partial P_{mn}^{ij}}, \frac{\partial \Pi}{\partial R_{mn}^{ij}}, \frac{\partial \Pi}{\partial S_{mn}^{ij}}, \frac{\partial \Pi}{\partial V_{mn}^{ij}} = 0 \quad \begin{cases} m = 1, 2, ..., M \\ n = 1, 2, ..., N \end{cases} \ . \quad (14)$$

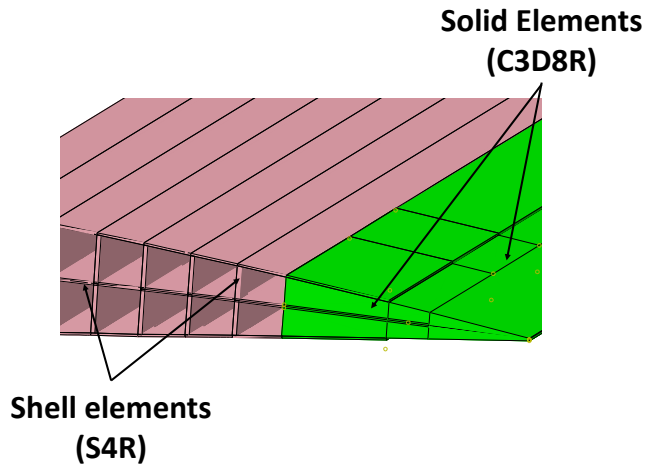

Fig. 6 A combination of shell and solid elements are used to model the complex FishBAC structure in Abaqus/CAE FEA software

This analytical model represents a fast approach to modelling the behaviour of the FishBAC morphing device using 1% of degrees of freedom (DOFs) — compared to Finite Element Analysis (FEA). Due to multi-plate assembly procedure and its mesh-independence, this model allows for simple, fast, parameter driven analysis of new FishBAC configurations. The authors have used this approach to automate the generation of entire FishBAC geometries from simple vectorised inputs of geometry and material properties — allowing for easy modification of the dimensions, aerofoil, detailed component geometries, material properties, stacking sequence, etc. without major impact on the convergence of the model.

IV. Numerical Validation: Finite Element Analysis

A Finite Element Analysis (FEA) model was developed in Abaqus/CAE 6.14 using a combination of shell and solid elements (Fig. 6). The composite bending plate, the stringers and the skin are modelled using four-node shell elements (S4R), while the thick non-morphing sections of the FishBAC are modelled using solid eight-node elements (C3D8R). In terms of material definitions, the spine is modelled as a composite laminate — on a ply-by-ply basis — and the stringers, solid trailing edge sections and skin are modelled as isotropic regions.

A fully clamped boundary condition is applied at the root of the FishBAC and the actuation loads are introduced as distributed moments at the spanwise locations anchor points of the drive tendon to the trailing edge. To validate the analytical model, displacements are tracked along all three free edges of the FishBAC at the nodes located at the centre of the spine (in the through-thickness direction). The actuation loads are applied as point moments at two external reference points, which are then coupled via *Kinematic Coupling* to the node sets that correspond to the actuation tendons. This coupling simulates a distributed actuation moment.

Finally, a mesh-convergence study was performed by tracking tip displacements when the overall element size was reduced from 10 mm to 2.5 mm (in increments of 2.5 mm). The mesh was considered to be converged when both tip displacements varied by less than 0.5%, with respect to the previous meshing iteration.

V. Composite FishBAC: Wind Tunnel Model

This section introduces the characteristics of a composite FishBAC wind tunnel model, which is the structure that is modelled in this study. The main structure corresponds to the first ever composite-spine carbon fibre FishBAC, which has been designed and manufactured for wind tunnel testing. The wind tunnel model is a rectangular planform NACA 23012 wing with a chord of 69 mm and a span of 1000 mm, with the FishBAC occupying the aft 69 mm of the chord. It has two actuation points with tendons mounted 415 mm from the centre of the wing: one on the left hand side (M_{x_2}) and one on the right hand side (M_{x_4}), when viewed from above. Fig. 7 shows a schematic diagram of this structural configuration and its primary dimensions.

A. Wind Tunnel Model

The tunnel model was designed and manufactured using a combination of metallic and 3D-printed plastic parts, with silicone sheet skins and a carbon fibre spine. The spine was manufactured using Hexcel®'s 8552/IM7 carbon fibre prepreg under vacuum bag and autoclave pressure curing. With a total cured ply thickness of 0.39 mm, this composite FishBAC provides another level of

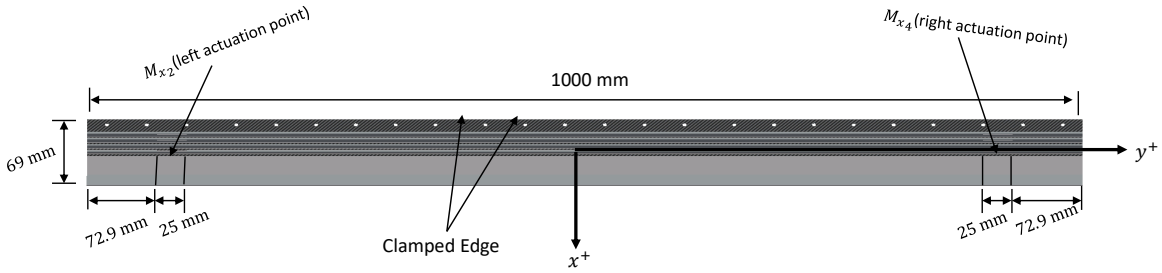

Fig. 7 FishBAC wind tunnel model global dimensions and actuation points

anisotropy — beyond what the plate-stringer configuration provides — as it has a layup ($[90/0/90]_T$), which produces low chordwise bending stiffness to minimise actuation requirements while maintaining spanwise stiffness to reduce elastic washout.

A series of 3D-printed plastic stringers and solid trailing edge sections were bonded to the cured composite spine using Cyanoacrylate adhesive. Whereas the use of plastic for the stringers implies that the spanwise bending stiffness of this FishBAC will be significantly lower than a fully composite version, the choice was made to use 3D printed polymer to reduce the complexity and risk of this first attempt at a composite FishBAC. This will significantly increase the amount of elastic washout of deformation which occurs along the span (particularly for more highly loaded cases), but this can be readily addressed in future designs. The structure is actuated at two locations using a total of four KST X10 HV servo actuators — two in each location [30]. As mentioned above, the actuation loads are transferred to the spine by a pulley-tendon system using a Kevlar-tape tendon that is stitched to the carbon plate. Finally, a pre-tensioned elastomeric silicone sheet covers the FishBAC structure and provides the aerofoil shape. Fig. 8 shows a close-up view of the composite FishBAC morphing device — note that the fairing that covers the very rear of the trailing edge has been removed.

B. Material Characterisation

In order to accurately predict the deflections of the FishBAC, a material characterisation was performed to obtain experimental stiffness and Poisson's ratio values. The carbon fibre used for this material characterisation was cured in the same vacuum bag as the FishBAC spine, thus, underwent the same curing cycle.

The carbon fibre's 0° and 90° Young's modulus are determined in accordance with ASTM D3039 test standard [31], while the in-plane shear modulus is determined using ASTM D3518's test standard [32]. Furthermore, the ABS 'like' 3D-printed plastic was tested by following ASTM D638's test standard guidelines [33]. Finally, the silicone skin was tested using 25 mm × 150 mm samples, which where bonded to 3D-printed ABS end tabs to not only test the Young's modulus of the silicone skin, but also to test the adhesive that was used to bond the skin on the FishBAC wing. Tables 2 and 3 present the results of these material tests, which are the material properties that are used in both analytical and FEA models.

Fig. 8 Composite FishBAC device used for experimental validation of the analytical structural model

Table 2 Material properties of the 8552/IM7 carbon fibre prepreg. Properties obtained via tensile tests

Material	E_{11} [GPa]	E_{22} [GPa]	G_{12} [GPa]	ν_{12}
8552/IM7 Carbon Fibre	169.50	8.58	5.03	0.28

Table 3 Material properties of Isotropic silicone and ABS plastic. Properties obtained via tensile tests

Material	E [MPa]	G [MPa]	ν
40° Shore Silicone	1.18	0.427	0.38
ABS Plastic	2100	0.355	774.91

VI. Results and Model Improvements

The Mindlin-Reissner discontinuous plate model that is presented in this article is validated against Finite Element Analysis (FEA). This comparison is performed in terms of the percentage error difference along the spanwise free edge. Besides obtaining displacement fields under several load cases, two convergence studies were performed: the first one, to estimate the required number of polynomial terms to achieve convergence and the second one, to determine the stiffness of the artificial penalty springs. The stacking sequence and geometrical dimensions used correspond to the FishBAC wind tunnel model (i.e. stacking sequence of $[90°/0°/90°]_T$ and spine thickness of $t = 0.39\,\text{mm}$).

The FishBAC structure is discretised 16 chordiwise and 5 spanwise partitions of uniform thickness. These 16 chordwise partitions capture the presence of the stringers and the geometric taper of the aerofoil by using the average height between the start and end of each partition. Note that the structure could be discretised in more partitions, however, each additional partition increases the size of the system of equations (Eq. (14)).

A. Analytical Model: Polynomial term convergence

A convergence study was performed to determine the number of Chebyshev Polynomial terms needed to capture the deformed shapes with sufficient accuracy while avoiding unnecessary computational cost. In this study, the same FishBAC geometrical configuration was used and, for simplicity purposes, the number of chordwise and spanwise terms in each plate segment are equal to each other (although more plate segments are used along the span then along the chord). To assess convergence, both maximum and root-mean-square (RMS) percentage errors are calculated along the free spanwise edge. The chosen load case for this convergence study is a differential moment input of $M_{x_2} = -1\,\text{N m}$ and $M_{x_4} = 1\,\text{N m}$, respectively. This corresponds to the load case that the Kirchhoff-Love model was unable to model, while the selected moment magnitudes yield to deflections that are similar to the maximum ones that can be achieved by the composite wind tunnel prototype.

Table 4 shows a summary of the corresponding percentage errors, while Fig. 9 also shows the stability of the system of equations — in terms of the condition number *— and the total computational time per iteration. It is important to note that all these results were computed on a single Intel® Core™ i7-4790 3.60 GHz CPU processor, using a 64-bit OS with 32 GB of physical memory. Results show an early convergence within 4.2% and 2.7% maximum and RMS percentage errors, respectively, with as few as three polynomial terms in each direction. It can also be observed that increasing the number of terms only reduces both errors by a maximum of $\approx 1\%$. Furthermore, results show that the maximum error has a minimum value at five polynomial terms, and then increases with additional terms. This is due to the increase in condition number of the coefficient matrix when the number of polynomial terms is increased, as the system becomes more sensitive to small changes in stimuli. It can be concluded from this convergence study that this model, converges at five Chebyshev Polynomial terms, for this combination of material and geometrical properties.

B. Penalty Stiffness Convergence

A second convergence study was performed to determine the impact that the stiffness values chosen for the artificial penalty springs have on the stability of the solution. To assess this, the spanwise RMS error and the condition number are calculated for different penalty stiffness values. Fig. 10 shows the results of this convergence study, where it can be seen that the solution remains stable in terms of percentage error for penalty spring stiffnesses between $k = 10^6$ and $k = 10^{13}$. This is consistent with other structural models that implement this technique [20, 26, 36]. Furthermore, a minimum percentage error is observed when the penalty stiffness is $k = 10^6$, however, this value may vary depending on the geometric and material configuration, as well as the number of polynomial terms. Consequently, it is considered that a value of $k = 10^7$ guarantees convergence throughout this study, as it presents a stable condition number and low percentage error. Therefore, a value of $k = 10^7$ is used during the rest of this study.

*The condition number of a matrix is defined as the product of the Euclidean norm of the matrix and its inverse, such that $\kappa(A) = \|A\|\|A^{-1}\|$. A high condition number indicates an 'ill-conditioned' system, which are more sensible to changes in response due to small changes in stimuli [34, 35].

Table 4 Comparison of Analytical and geometrically linear FEA results in function of Chebyshev Polynomials terms (polynomial order).

Laminate	Material	Polynomial Terms (M=N)	Max. Error (Abs. Value) [%]	RMS Error [%]	DOF
$[90°/0°/90°]_T$	8552/IM7 Carbon Fibre	2	99.90	43.00	1600
		3	4.172	2.688	3600
		4	3.478	1.879	6400
		5	3.287	1.686	10000
		6	5.740	1.645	14400
		7	5.728	1.618	19600
		8	5.097	1.465	25600

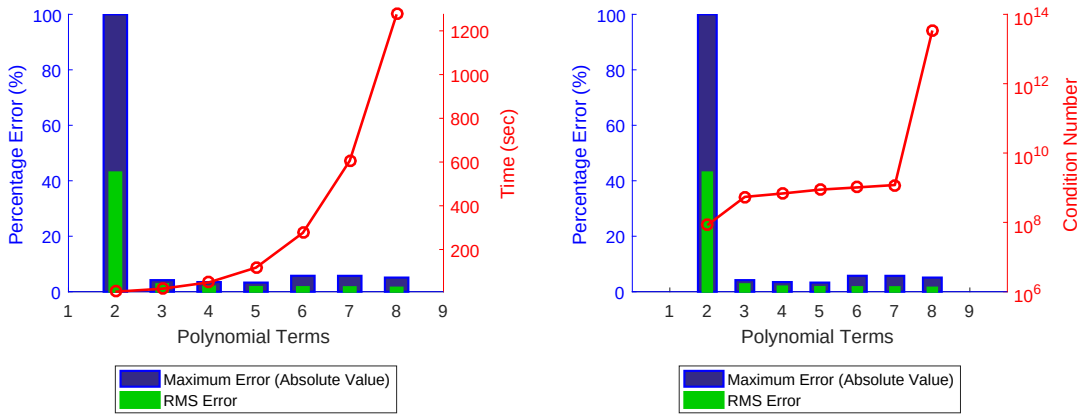

Fig. 9 Convergence study of analytical Mindlin-Reissner plate model versus Finite Element Analysis. Study also analysed the stability of the system — in terms of the condition number — and the total computation time of each iteration

C. Kirchhoff-Love vs. Mindlin-Reissner Model

The presented discontinuous Mindlin-Reissner model was primarily developed to address the inability of a discontinuous Kirchhoff-Love plate theory to capture deflections when differential actuation loads are applied (i.e. actuation moment loads with opposite direction). It was determined that this inability was due to the presence of transverse shear, as the structure reacts this load case by twisting, which induces transverse shear on the yz-plane. Since Kirchhoff-Love models cannot capture transverse shear deformations, a First-Order Transverse Shear Deformation (FTSD) approach was implemented. Fig. 11 shows a direct comparison between Kirchhoff-Love, Mindlin-Reissner and FEA models, when the FishBAC is loaded under differential actuation (i.e. equal magnitude but opposite direction). On one hand, it can be observed that the Kirchhoff-Love model fails to predict the FishBAC displacement (compared to FEA), presenting a RMS percentage error — along the spanwise edge — of 35 %. On the other hand, it can be observed that the Mindlin-Reissner model successfully captures the displacement of the FishBAC, presenting an RMS percentage error of less than 2%. This result highlights the importance of developing this new model, which will be used for further design, optimisation and fluid-structure interaction of this morphing concept.

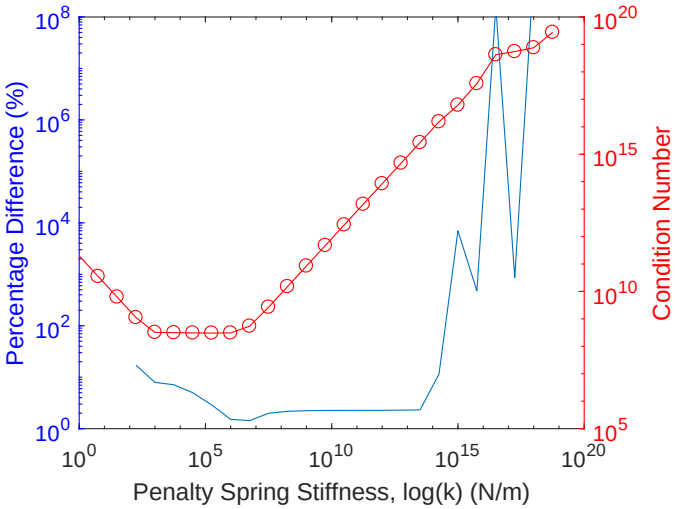

Fig. 10 Root-mean-square error — along the spanwise edge — and condition number, in function of penalty spring stiffness. Note that, for values lower than $k = 10^2$, there is no solution as the coefficient matrix is singular.

D. Comparison Study: Mindlin-Reissner vs. FEA

A more thorough comparison study of FEA vs. analytical displacement fields is performed. Three different load cases are considered depending on the actuation torque inputs: uniform actuation (i.e. equal magnitude and direction), differential actuation (i.e. equal magnitude, but opposite direction) and single input (i.e. only one actuation input instead of two). The following subsection introduces these results.

1. Uniform Actuation

The uniform actuation case corresponds to equal actuation inputs — in magnitude and direction — at both actuation points located at each spanwise edge of the FishBAC device. The FishBAC reacts these uniform actuation loads in pure bending. Figs. 12 and 13 show a comparison between analytical and FEA results, showing an agreement with a maximum and RMS percentage error — along the spanwise edge — of 12.94% and 7.485%, respectively. One important characteristic of these displacement fields is the significant elastic washout along the span, which both models are able to capture. As mentioned above, this is due to the use of plastic instead of carbon fibre composite for the stringers in the wind tunnel model. While future designs will most likely be stiffer in the spanwise direction, the ability to capture the washout created by spanwise compliance is still crucial to the efficacy of this model, as washout will significantly impact the aerodynamic performance.

2. Single Actuation Input

This load case corresponds to having actuation input to only one actuation point. To simulate this case, a negative actuation input between $M_{x_4} = -0.25\,\mathrm{N}\cdot\mathrm{m}$ and $M_{x_4} = -1\,\mathrm{N}\cdot\mathrm{m}$ was applied at the right-end actuation point, while the other actuation input was set to zero. Fig. 14 shows these results, which present a maximum and RMS error — along the spanwise edge — of 13.70% and 9.132%, respectively. This actuation case is primarily reacted as bending on the chordwise direction, with significant displacement variations along the span. This type of actuation case could potentially be useful for controlling spanwise aerodynamic loads, as different lift distributions along the span can be obtained.

3. Differential Actuation

The differential actuation case consists of applying equal magnitude torque inputs in both actuation points, but with opposite directions. This causes a net torque on the FishBAC structure, inducing transverse shear. Consequently, this scenario cannot be accurately captured using Kirchhoff-Love Plate Theory.

Actuation inputs of magnitudes between M_x =0.25 N m and M_x =1 N m, in increments of 0.25 N m, are applied. Fig. 15 shows the displacement fields obtained using both FEA and analytical model. It can be observed that the FEA and analytical results agree with each other (Fig. 15), with a maximum and RMS percentage error — along the free spanwise edge — of 3.28% and 2%, respectively. This is a significant improvement from the Kirchhoff-Love model, which presents a RMS percentage error of 33%.

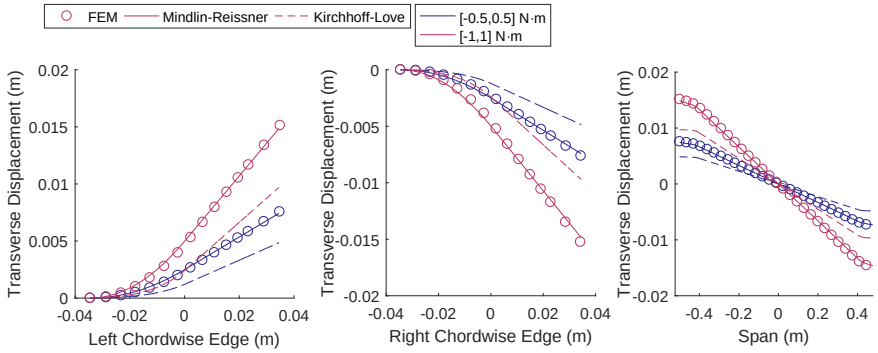

Fig. 11 Comparison between Kirchhoff-Love and Mindlin-Reissner discontinuous plate models and Finite Element Analysis (FEA)

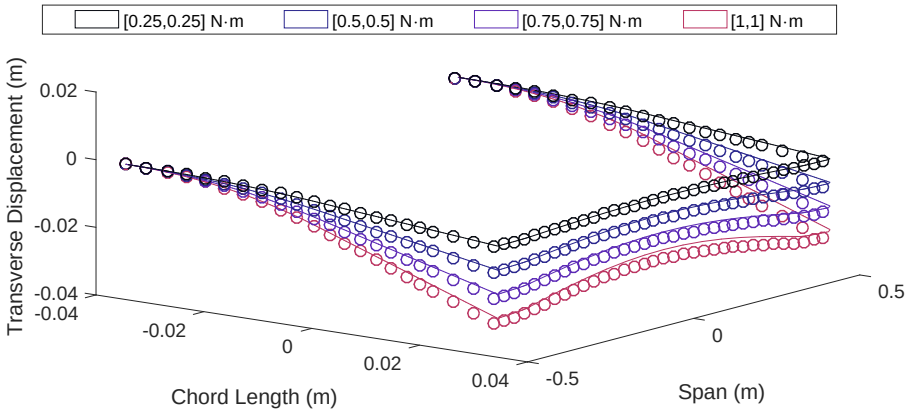

Fig. 12 Mindlin-Reissner discontinuous plate model vs. FEA under uniform actuation loads (trailing edge down)

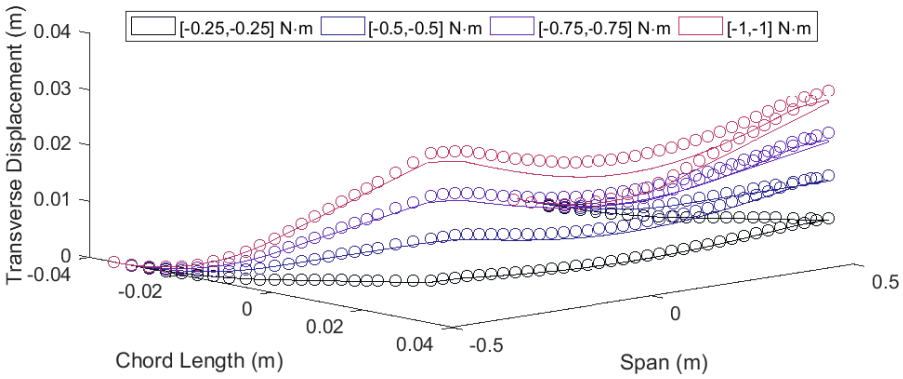

Fig. 13 Mindlin-Reissner discontinuous plate model vs. FEA under uniform actuation loads (trailing edge up)

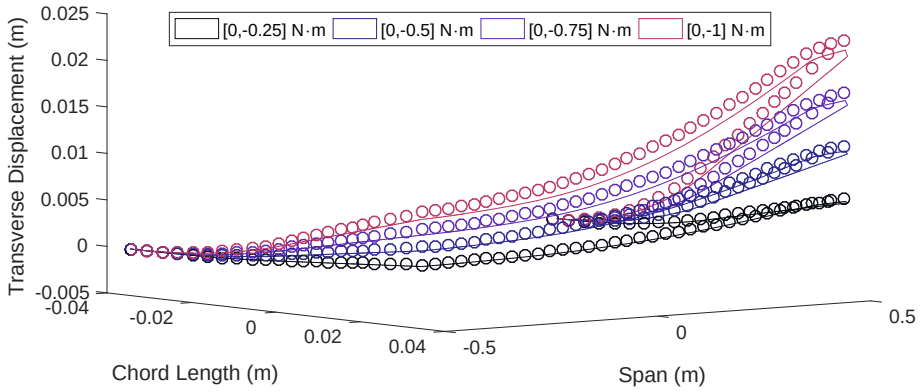

Fig. 14 Mindlin-Reissner discontinuous plate model vs. FEA under a single actuation load

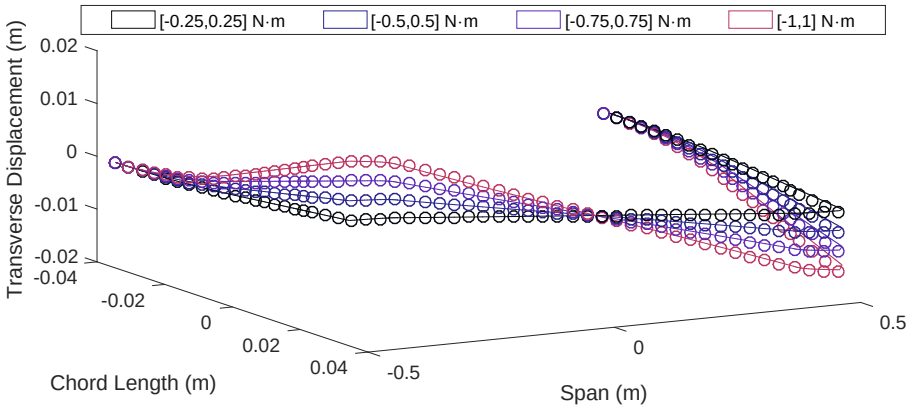

Fig. 15 Mindlin-Reissner discontinuous plate model vs. FEA under differential actuation loading (i.e. equal moment magnitude but opposite directions)

E. Numerical Efficiency

This subsection summarises the presented work by evaluating the total percentage errors of the Mindlin-Reissner model — with respect to FEA — and by estimating the total number of degrees of freedom (DOFs) that each solution requires for convergence. Table 5 shows a summary of these degrees of freedom (DOFs) required for convergence. Furthermore, it shows the maximum RMS percentage error that both analytical models have, with respect to FEA. It can be observed that the number of DOFs increases by 66% when transverse shear is modelled, however these are still a fraction (around 1%) of the FEA DOFs' required for convergence.

Furthermore, a summary of the comparison study between the Mindlin-Reissner discontinuous plate model and FEA is presented in Table 6. It can be observed that the maximum RMS error occurs when a single actuation input is applied. This maximum percentage error of $\approx 9\%$ is a significant improvement from the errors between 35% and 45% obtained using a Kirchhoff-Love discontinuous plate model [20].

Table 5 Efficiency study, in terms of required degrees of freedom (DOFs) for convergence

Model	DOFs	RMS Error [%]
FEA	1,086,426	–
Kirchhoff-Love	6,000	35.42
Mindlin-Reissner	10,000	9.13

Table 6 Maximum RMS error of Mindlin-Reissner discontinuous plate model, under different load cases. Errors are calculated with respect to Finite Element Analysis

Load Case	RMS Error [%]	Maximum Error[%]
Symmetric	7.485	12.94
Single-Input	9.132	13.70
Differential	2.128	3.28

VII. Conclusion

A discontinuous, mesh-independent Mindlin-Reissner plate model was developed to model the highly anisotropic composite FishBAC morphing device. The novelty of this model lies on its ability to fully capture both chordwise and spanwise transverse shear displacements of the FishBAC — when subjected to different load cases — using only a fraction (around 1%) of the degrees of freedom a FEA model needs. This model addresses the limitations of a previously developed Kirchhoff-Love plate model, which failed to predict the FishBAC's behaviour at certain load cases due to its inability to account for transverse shear strains.

One of the main advantages of this model is that it converges on a fixed number of degrees of freedom, it does not require meshing and all the polynomial integrals can be calculated once up-front, then simply retrieved from a lookup table during analysis, which means that all the computationally expensive steps are performed in advance. A summary of the main findings of this study is given as follows:

1) The Mindlin-Reissner plate theory-based model is able to accurately predict the out-of-plane displacement of the FishBAC when the structure is subject to twist, with a percentage error of $\approx 2\%$ when compared to FEA.
2) The worst-case RMS error between the Mindlin-Reissner plate model and the numerical (FEM) solution is of approximately 9%, with typical RMS error values of 2-7%.
3) The Mindlin-Reissner plate model converges using 99 % fewer Degrees of Freedom (DOFs) than the Finite Element Analysis approach. It is mesh-independent, parametrically defined computationally efficient and can be used to model any continuous or discontinuous anisotropic plate structure subject to changes in thickness along either of the in-plane dimensions.

Future work using this model will include further design refinement and optimisation of the FishBAC, as well as fluid-structure interaction of this promising camber morphing composite device to fully capture its coupled aeroelastic behaviour.

Acknowledgments

This work was supported by the Engineering and Physical Sciences Research Council through the EPSRC Centre for Doctoral Training in Advanced Composites for Innovation and Science [grant number EP/L016028/1].

Furthermore, this project has received funding from the European Union's Horizon 2020 research and innovation programme under grant agreement No. 723491.

Paul M. Weaver would like to acknowledge the Royal Society for the Royal Society Wolfson Merit award.

Data Access Statement

All underlying raw data used in this study are available for download from the Research Data Repository of University of Bristol, data.bris, at: https://data.bris.ac.uk/data/dataset/2e8tk1wqyjmat2tvyk8fn2fb3h

References

[1] Barbarino, S., Bilgen, O., Ajaj, R. M., Friswell, M. I., and Inman, D. J., "A Review of Morphing Aircraft," *J. Intell. Mater. Syst. Struct.*, Vol. 22, No. 9, 2011, pp. 823–877. doi:10.1177/1045389X11414084.

[2] Woods, B. K., Bilgen, O., and Friswell, M. I., "Wind tunnel testing of the fish bone active camber morphing concept," *J. Intell. Mater. Syst. Struct.*, Vol. 25, No. 7, 2014, pp. 772–785. doi:10.1177/1045389X14521700.

[3] Sofla, A., Meguid, S., Tan, K., and Yeo, W., "Shape morphing of aircraft wing: Status and challenges," *Mater. Des.*, Vol. 31, No. 3, 2010, pp. 1284–1292. doi:10.1016/j.matdes.2009.09.011, URL `http://linkinghub.elsevier.com/retrieve/pii/S0261306909004968`.

[4] Beaverstock, C., Woods, B., Fincham, J., and Friswell, M., "Performance Comparison between Optimised Camber and Span for a Morphing Wing," *Aerospace*, Vol. 2, No. 3, 2015, pp. 524–554. doi:10.3390/aerospace2030524, URL `http://www.mdpi.com/2226-4310/2/3/524/`.

[5] Parker, H., "The Parker Variable Camber," Tech. Rep. 77, National Advisory Committee for Aeronautics, Washington, DC, 1920.

[6] Hogan, H. J., "Variable Camber Airfoil," *U.S. Pat. 1 ,868,748*, 1932.

[7] Chilton, R., "Variable Area-and-Camber Wing," *U.S. Pat. 2,222,935*, 1940.

[8] Bilgen, O., Friswell, M. I., Kochersberger, K. B., and Inman, D. J., "Surface Actuated Variable-Camber and Variable-Twist Morphing Wings Using Piezocomposites," *Struct. Struct. Dyn. Mater. Conf.*, Vol. 19, No. April, 2011, pp. 1–13. doi:10.2514/6.2011-2072.

[9] Kota, S., Hetrick, J. A., Osborn, R., Paul, D., Pendleton, E., Flick, P., and Tilmann, C., "Design and application of compliant mechanisms for morphing aircraft structures," , No. August 2003, 2003, p. 24. doi:10.1117/12.483869, URL http://proceedings.spiedigitallibrary.org/proceeding.aspx?doi=10.1117/12.483869.

[10] Barbarino, S., Pecora, R., Lecce, L., Concilio, A., Ameduri, S., and Calvi, E., "A novel SMA-based concept for airfoil structural morphing," *J. Mater. Eng. Perform.*, Vol. 18, No. 5-6, 2009, pp. 696–705. doi:10.1007/s11665-009-9356-3.

[11] Diaconu, C. G., Weaver, P. M., and Mattioni, F., "Concepts for morphing airfoil sections using bi-stable laminated composite structures," *Thin-Walled Struct.*, Vol. 46, No. 6, 2008, pp. 689–701. doi:10.1016/j.tws.2007.11.002.

[12] Daynes, S., Nall, S., Weaver, P., Potter, K., Margaris, P., and Mellor, P., "Bistable Composite Flap for an Airfoil," *J. Aircr.*, Vol. 47, No. 1, 2010, pp. 334–338. doi:10.2514/6.2009-2103, URL http://arc.aiaa.org/doi/abs/10.2514/6.2009-2103.

[13] De Gaspari, A., and Ricci, S., "A Two Levels Approach for the Optimal Design of Morphing Airfoils," *13th AIAA/ISSMO Multidiscip. Anal. Optim. Conf.*, Vol. 9388, No. 13 - 15 September 2010, Fort Worth, Texas, 2010. doi:10.2514/6.2010-9388.

[14] Vasista, S., Riemenschneider, J., van de Kamp, B., Monner, H. P., Cheung, R. C. M., Wales, C., and Cooper, J. E., "Evaluation of a Compliant Droop-Nose Morphing Wing Tip via Experimental Tests," *J. Aircr.*, Vol. 54, No. 2, 2017, pp. 519–534. doi:10.2514/1.C033909, URL https://arc.aiaa.org/doi/10.2514/1.C033909.

[15] Larson, R. R., "Flight Control System Development and Flight Test Experience With the F-111 Mission Adaptive Wing Aircraft," Tech. rep., NASA Ames Research Center, Edwards, California, 1986.

[16] Kudva, J. N., "Overview of the DARPA Smart Wing Project," *J. Intell. Mater. Syst. Struct.*, Vol. 15, No. 4, 2004, pp. 261–267. doi:10.1177/1045389X04042796.

[17] Campanile, L. F., and Sachau, D., "Belt-rib concept: a structronic approach to variable camber," *J. Intell. Mater. Syst. Struct.*, Vol. 11, No. 3, 2000, pp. 215–224. doi:10.1106/6H4B-HBW3-VDJ8-NB8A.

[18] Woods, B. K. S., and Friswell, M. I., "Preliminary Investigaion of a Fishbone Active Camber Concept," *ASME Conf. Smart Mater. Adapt. Struct. Intell. Syst.*, 2012. doi:10.1017/CBO9781107415324.004.

[19] Rivero, A. E., Weaver, P. M., Cooper, J. E., and Woods, B. K., "Progress on the Design , Analysis and Experimental Testing of a Composite Fish Bone Active Camber Morphing Wing," *ICAST 2017 28th Int. Conf. Adapt. Struct. Technol.*, Cracow, Poland, 2017, pp. 1–11.

[20] Rivero, A. E., Weaver, P. M., Cooper, J. E., and Woods, B. K., "Parametric structural modelling of fish bone active camber morphing aerofoils," *J. Intell. Mater. Syst. Struct.*, 2018, p. 1045389X1875818. doi:10.1177/1045389X18758182, URL http://journals.sagepub.com/doi/10.1177/1045389X18758182.

[21] Coburn, B. H., Wu, Z., and Weaver, P. M., "Buckling analysis of stiffened variable angle tow panels," *Compos. Struct.*, Vol. 111, No. 1, 2014, pp. 259–270. doi:10.1016/j.compstruct.2013.12.029, URL http://dx.doi.org/10.1016/j.compstruct.2013.12.029.

[22] Whitney, J. M., *Structural Analysis of Laminated Anisotropic Plates*, Technomic Publishing, Lancaster, Pennsylvania, 1987.

[23] Ilanko, S., Monterrubio, L., and Mochida, Y., *The Rayleigh-Ritz Method for Structural Analysis*, Iste Series, Wiley, London and New York, 2015.

[24] Timoshenko, S. P., "LXVI. On the correction for shear of the differential equation for transverse vibrations of prismatic bars," *Philos. Mag. Ser. 6*, Vol. 41, No. 245, 1921, pp. 744–746. doi:10.1080/14786442108636264.

[25] Oñate, E., *Thick/Thin Plates. Reissner-Mindlin Theory*, Springer Netherlands, Dordrecht, 2013, pp. 291–381. doi:10.1007/978-1-4020-8743-1_6, URL https://doi.org/10.1007/978-1-4020-8743-1{_}6.

[26] Coburn, B. H., "Buckling of stiffened variable stiffness panels," Phd thesis, University of Bristol, 2015.

[27] Hyer, M. H., *Stress Analysis of Fiber-Reinforced Composite Materials*, McGraw-Hill, New Delhi, 2014.

[28] Jaunky, N., Knight, N., and Ambur, D., "Buckling of arbitrary quadrilateral anisotropic plates," *AIAA J.*, Vol. 33, No. 5, 1995, pp. 938–944. doi:10.2514/3.12512, URL http://dx.doi.org/10.2514/3.12512.

[29] Groh, R. M., and Weaver, P. M., "Static inconsistencies in certain axiomatic higher-order shear deformation theories for beams, plates and shells," *Compos. Struct.*, Vol. 120, 2015, pp. 231–245. doi:10.1016/j.compstruct.2014.10.006, URL http://dx.doi.org/10.1016/j.compstruct.2014.10.006.

[30] KST, "X10 Wing Servo," , 2017. URL https://www.hyperflight.co.uk/getfile.asp?code=KST-X10{&}code2=1.

[31] D3039, "Standard Test Method for Tensile Properties of Polymer Matrix Composite Materials," *ASTM Int.*, Vol. 08, 2014, pp. 1–13. doi:10.1520/D3039.

[32] D3518, "Standard Test Method for In-Plane Shear Response of Polymer Matrix Composite Materials by Tensile Test," *ASTM Int.*, Vol. 94, No. Reapproved, 2007, pp. 1–7. doi:10.1520/D3518.

[33] D638, "Standard test method for tensile properties of plastics," *ASTM Int.*, , No. C, 2013, pp. 1–16. doi:10.1520/D0638-10.1.

[34] G.W. Steward, J. W. A. C. C. M., "An Estimate for the Condition Number of a Matrix," *SIAM J. Appl. Math.*, Vol. 16, No. 2, 1979, pp. 368–375.

[35] Groh, R. M., "Non-classical effects in straight-fibre and tow-steered composite beams and plates," Phd thesis, University of Bristol, 2015.

[36] Vescovini, R., and Bisagni, C., "Buckling analysis and optimization of stiffened composite flat and curved panels," *AIAA J.*, Vol. 50, No. 4, 2012, pp. 904–915. doi:10.2514/1.J051356.